PERGAMON

International Journal of Solids and Structures 39 (2002) 879–895

INTERNATIONAL JOURNAL OF SOLIDS and STRUCTURES

www.elsevier.com/locate/ijsolstr

A nonlinear finite element formulation for axisymmetric torsion of biphasic materials

X.N. Meng [a], M.A. LeRoux [b], T.A. Laursen [a,*], L.A. Setton [b]

[a] *Department of Civil and Environmental Engineering, Duke University, Box 90287, 127 Hudson Hall, Durham, NC 27708-0287, USA*

[b] *Department of Biomedical Engineering, Duke University, Durham, NC 27708-0281, USA*

Received 21 April 2001

Abstract

In this paper, we present a finite element formulation for describing the large deformation torsional response of biphasic materials, with specific application to prediction of nonlinear coupling between torsional deformation and fluid pressurization in articular cartilage. Due to the use of a cylindrical coordinate system, a particular challenge arises in the linearization of the weak form. The torsional axisymmetric case considered gives rise to additional geometric terms, which are important for the robustness of the numerical implementation and that would not be present in a Cartesian formulation. A detailed derivation of this linearization process is given, couched in the context of a variational formulation suitable for finite element implementation. A series of numerical parametric studies are presented and compared to experimental measurements of the time dependent response of cartilage.

Keywords: Nonlinear finite element analysis; Biphasic theory; Articular cartilage; Viscoelastic behavior; Torsional behavior

1. Introduction

Articular cartilage is a porous, hydrated material that exhibits flow-dependent viscoelastic effects when loaded, including interstitial fluid pressurization and fluid flow (Mow et al., 1980; Soltz and Ateshian, 2000, 1998). Compositionally, articular cartilage consists of a polymeric solid phase of largely collagen and proteoglycan macromolecules, and interstitial fluid phase consisting largely of water and dissolved solutes. The mechanical behaviors of this tissue have been well described by a multiphasic theoretical formulation (Bowen, 1998; Truesdell and Toupin, 1960) that accounts for mechanical interactions between these solid and fluid phases (Mow et al., 1980). Analytical solutions of the biphasic theoretical model have been shown to capture important physical characteristics of cartilage when subjected to compressive loading in simplified one and two-dimensional axisymmetric configurations (Mow et al., 1980; Armstong et al., 1986; Mak et al., 1987). Finite element implementations of the linear biphasic theoretical model or linear

* Corresponding author. Tel.: +1-919-660-5430; fax: +1-919-660-5219.
E-mail address: laursen@duke.edu (T.A. Laursen).

0020-7683/02/$ - see front matter
PII: S0020-7683(01)00249-9

poroelasticity have also been developed to study articular cartilage in more complex loading configurations and sample geometries (Spilker et al., 1990; Suh et al., 1991; Levenston et al., 1998; Wayne et al., 1991). All of these codes have demonstrated an ability to predict important flow-dependent viscoelastic behaviors for cartilage when subjected to compressive loading.

Cartilage is also known to exhibit significant viscoelastic effects in response to torsional shear (Hayes and Mockros, 1973; Zhu et al., 1995; Setton et al., 1995). Within linear theory, the solid matrix of cartilage is predicted to experience zero dilatation for small angles of deformation, and so will not experience any associated flow-dependent effects such as fluid pressurization and fluid flow. Thus, the viscoelastic effects observed in torsional shear have been attributed to a flow-independent mechanism arising from physical interactions between polymeric molecules of the solid phase (Hayes and Mockros, 1973; Mak, 1986). Recently, experimental studies have demonstrated that a significant, transient normal force may be generated in articular cartilage when subjected to pure torsion in either steady shearing or stress-relaxation testing (LeRoux et al., 1999, 2000). In these experiments, cylindrical axisymmetric samples of articular cartilage were subjected to torsional displacements while the axial, or normal force was recorded for the duration of this prescribed torsional loading. A significant, nonzero normal stress was generated in response to torsional deformation that is hypothesized to contribute to load-bearing mechanisms for the tissue. The kinetics of the normal force transients are similar to the shear stress transients in the stress-relaxation experiment (LeRoux et al., 1999), suggesting that a coupling mechanism exists between viscoelastic effects in pure torsion and normal stress. In linear theory, the rotation is always decoupled from radial and axial displacements, however, with the result that a linear formulation of the pure torsion problem always generates zero dilatation and zero pressure in a biphasic material. In this paper, we present a novel finite element formulation of the finite deformation axisymmetric torsional problem to investigate the coupling between torsional and normal stress effects in a biphasic material.

In applying the finite element technique to a biphasic analysis, at least three different types of formulations have been implemented: two field *solid displacement-fluid velocity* penalty formulations (Spilker et al., 1990; Suh et al., 1991); two field *solid displacement-fluid pressure* formulations (Wayne et al., 1991); and multifield *variational* formulations (Levenston et al., 1998) with a Lagrangian multiplier (Almeida, 1995) or augmented Lagrangian multiplier approach. In the current study, a two field displacement–pressure formulation (*u–p* formulation) is used to study the torsional behavior of biphasic soft tissues, which precludes the need to invoke penalizations or Lagrange multipliers. In contrast to most of the above studies, we consider the *full finite strain response* of the solid matrix in this study. A challenge in the torsional axisymmetric finite element formulation we consider comes from the linearization of the weak form. In a curvilinear coordinate system, the process not only involves the linearization of the components of relevant tensors but also the linearization of variable bases, which will generate additional terms in the geometric stiffnesses (a simplified treatment of these terms is presented in (Celigoj, 1998). To our knowledge, these terms have not been incorporated in previous finite element formulations describing the finite deformation behavior of biphasic materials. Omitting these terms in the torsional problem will, in general, cause a loss of quadratic rates of convergence of the Newton–Raphson method while solving the nonlinear system of discrete equations. In the current work, we present a detailed derivation of the formulation and its linearization, and demonstrate that the resulting numerical tool can be used to predict the coupling between pure torsion and normal stress effects in articular cartilage.

2. Continuum mechanics preliminaries

A biphasic material is considered to consist of two intrinsically incompressible and immiscible phases, denoted by $\alpha = s, f$ for solid and fluid phases respectively (Mow et al., 1980). In terms of Cauchy stress, the momentum equation for the αth phase, in the absence of body forces and inertia effects, is given by

$$\nabla \cdot \boldsymbol{\sigma}^{\alpha} + \boldsymbol{\pi}^{\alpha} = 0 \tag{1}$$

with the stress tensor for each individual phase defined as

$$\begin{aligned} \boldsymbol{\sigma}^{\mathrm{s}} &= -\phi^{\mathrm{s}} p \boldsymbol{I} + \boldsymbol{\sigma}^{\mathrm{e}}, \\ \boldsymbol{\sigma}^{\mathrm{f}} &= -\phi^{\mathrm{f}} p \boldsymbol{I}, \end{aligned} \tag{2}$$

where ϕ^{α} denotes the current volume fraction of the αth phase, p denotes the fluid pressure and $\boldsymbol{\sigma}^{\mathrm{e}}$ is the effective stress tensor for the solid matrix of the material. $\boldsymbol{\pi}^{\alpha}$ is a diffusive drag interaction term, defined as

$$\boldsymbol{\pi}^{\mathrm{f}} = \boldsymbol{K}(\boldsymbol{v}^{\mathrm{f}} - \boldsymbol{v}^{\mathrm{s}}) = -\boldsymbol{\pi}^{\mathrm{s}}, \tag{3}$$

where $\boldsymbol{K}$ is a diffusive drag tensor (Mow et al., 1980). In this formulation, the diffusive drag is related to the hydraulic permeability tensor as $\boldsymbol{k} = (\phi^{\mathrm{f}})^2 \boldsymbol{K}^{-1}$. In a u–p formulation, the balance of linear momentum for the solid and fluid phases may thus be written as

$$\sigma^{ij}_{;j} - g^{ik} p_{,k} = 0, \tag{4}$$

$$v^{(\mathrm{f/s})i} = -k^{ji} p_{,j}, \tag{5}$$

where σ^{ij} are the contravariant components of the effective stress in the solid phase (the superscript e has been dropped for convenience), p is the fluid pressure, g^{ik} are the contravariant components of the metric tensor, and $v^{(\mathrm{f/s})i} := \phi^{\mathrm{f}}(v^{(\mathrm{f})i} - v^{(\mathrm{s})i})$ are the contravariant components of the relative fluid velocity. In Eqs. (4) and (5), and in the sequel we use indicial notation, with repeated indices indicating implied summation and the use of the semicolon via $(\cdot)_{i;j}$ indicating covariant differentiation in a curvilinear coordinate system (in this case, this coordinate system will eventually correspond to an axisymmetric one).

The balance of mass for the αth phase is described by

$$\dot{\rho}^{\alpha} + \rho^{\alpha} v^{(\alpha)i}_{;i} = 0. \tag{6}$$

If one assumes saturation of the biphasic medium, as well as incompressibility, one also obtains:

$$\begin{aligned} \phi^{\mathrm{f}} + \phi^{\mathrm{s}} &= 1, \\ \gamma^{\alpha} &= \gamma^{\alpha}_{0}, \end{aligned} \tag{7}$$

where γ^{α}_{0} denotes the reference material density, or *intrinsic* density, for each phase. Combination of Eqs. (6) and (7) gives rise to the following continuity equation for the biphasic material

$$(\phi^{\mathrm{s}} v^{(\mathrm{s})i} + \phi^{\mathrm{f}} v^{(\mathrm{f})i})_{;i} = 0 \tag{8}$$

which is the constraint that typically appears in two field penalty formulations. By contrast, combining the momentum equation (8) and continuity equation (5) for the fluid phase leads to the equation used in a u–p formulation such as is employed here,

$$(v^{i} - k^{ij} p_{,j})_{;i} = 0, \tag{9}$$

where v^{i} are the contravariant components of the solid phase velocity (again for simplicity, the superscript s has been dropped). In our formulation, linear permeability is assumed, i.e., the permeability tensor is defined as $\boldsymbol{k} = k_0 \boldsymbol{I}$ with k_0 taken to be a constant and $\boldsymbol{I}$ denoting the second order identity tensor.

3. The biphasic weak form and its linearization

In what follows, let Ω denote the current configuration of a biphasic body and $\bar{\Omega} := \Omega + \partial\Omega$ indicate the closure of Ω, where the boundary $\partial\Omega$ can be partitioned as $\partial\Omega = \Gamma_\sigma + \Gamma_u$ and $\partial\Omega = \Gamma_p + \Gamma_Q$. We further assume that $\Gamma_\sigma \cap \Gamma_u = \emptyset$ and $\Gamma_p \cap \Gamma_Q = \emptyset$ (here, $\emptyset$ denotes the null space). The notations Γ_σ and Γ_u denote the regions where stresses and displacements (respectively) are specified on the boundary; correspondingly, Γ_p and Γ_Q are the regions where fluid pressures and fluxes are prescribed. The smooth manifold of admissible solutions is then defined by

$$\mathscr{Q} := \{\boldsymbol{u} \times p : \Omega_0 \to \Omega | \boldsymbol{u}_{|\Gamma_u} = \bar{\boldsymbol{u}}\ p_{|\Gamma_p} = \bar{p}\}. \tag{10}$$

Correspondingly, we define $\mathscr{V} \in H^1(\Omega)$ as the space of test functions associated with $\mathscr{Q}$, via

$$\mathscr{V} := \{\boldsymbol{w} \times q : \Omega_0 \to \Omega | \boldsymbol{w}_{|\Gamma_u} = 0\ q_{|\Gamma_p} = 0\}. \tag{11}$$

Application of the standard weighted residual procedure to Eqs. (4) and (9) leads to the following (coupled) weak form

$$\int_\Omega w_{i;j}\sigma^{ij}\,\mathrm{d}\Omega + \int_\Omega w_k g^{ik} p_{,i}\,\mathrm{d}\Omega = \int_{\Gamma_\sigma} w_i t^i\,\mathrm{d}\Gamma \tag{12}$$

and

$$\int_\Omega q v^i_{;i}\,\mathrm{d}\Omega + \int_\Omega q_{,i} k^{ij} p_{,j}\,\mathrm{d}\Omega = -\int_{\Gamma_Q} qQ\,\mathrm{d}\Gamma, \tag{13}$$

where $\boldsymbol{w}$ and q are the trial functions standing in the weighting space, and $t^i = \sigma^{ij} n_j$ and $Q = -k^{ij} p_{,j} n_i$ are the prescribed traction and fluid flux fields, respectively. In subsequent developments, it will prove convenient to summarize the coupled system summarized by Eqs. (12) and (13) via

$$\begin{aligned} G_1^{\mathrm{int}} + G_2^{\mathrm{int}} &= \int_{\Gamma_\sigma} w_i t^i\,\mathrm{d}\Gamma, \\ G_3^{\mathrm{int}} + G_4^{\mathrm{int}} &= -\int_{\Gamma_Q} qQ\,\mathrm{d}\Gamma, \end{aligned} \tag{14}$$

where G_1^{int} and G_2^{int} refer to the first and second terms in Eq. (12), while G_3^{int} and G_4^{int} are the first and second terms in Eq. (13).

When a Newton–Raphson procedure is chosen to solve this problem, a linearization of the weak form is required. Specifically, given an iterate i for the solution, denoted by $(\boldsymbol{u}^i, p^i)$, we solve linearized systems for displacement and pressure increments $(\Delta\boldsymbol{u}, \Delta p)$ according to

$$\begin{aligned} &G_1^{\mathrm{int}}(\boldsymbol{u}^i, p^i) + \Delta G_1^{\mathrm{int}}(\boldsymbol{u}^i, p^i) + G_2^{\mathrm{int}}(\boldsymbol{u}^i, p^i) + \Delta G_2^{\mathrm{int}}(\boldsymbol{u}^i, p^i) - \int_{\Gamma_\sigma} w_i t^i\,\mathrm{d}\Gamma = 0, \\ &G_3^{\mathrm{int}}(\boldsymbol{u}^i, p^i) + \Delta G_3^{\mathrm{int}}(\boldsymbol{u}^i, p^i) + G_4^{\mathrm{int}}(\boldsymbol{u}^i, p^i) + \Delta G_4^{\mathrm{int}}(\boldsymbol{u}^i, p^i) + \int_{\Gamma_Q} qQ\,\mathrm{d}\Gamma = 0, \end{aligned} \tag{15}$$

where ΔH denotes the sum of the directional derivatives of the functional H in the directions of $\Delta\boldsymbol{u}$ and Δp via

$$\Delta H := \Delta_u H + \Delta_p H = \frac{\mathrm{d}}{\mathrm{d}\epsilon}\bigg|_{\epsilon=0} H(\boldsymbol{u} + \epsilon\Delta\boldsymbol{u}, p) + \frac{\mathrm{d}}{\mathrm{d}\epsilon}\bigg|_{\epsilon=0} H(\boldsymbol{u}, p + \epsilon\Delta p). \tag{16}$$

Following solution of Eq. (15) for $\Delta \boldsymbol{u}$ and Δp, the solution is updated via

$$\boldsymbol{u}^{i+1} = \boldsymbol{u}^i + \Delta \boldsymbol{u}, \qquad p^{i+1} = p^i + \Delta p \tag{17}$$

and iterations on i are continued until convergence is obtained. A key intricacy of the implementation we present is the proper calculation of the linearizations indicated in Eq. (15). We now consider the linearization of these terms in detail.

In terms of the material configuration, G_1^{int} can be rewritten as

$$G_1^{\text{int}} = \int_{\Omega_0} w^i_{;j} \tau^j_i \, \mathrm{d}\Omega_0 = \int_{\Omega_0} w_{i;I} F^i_J S^{JI} \, \mathrm{d}\Omega_0, \tag{18}$$

where S^{JI} are the contravariant components of the second Piola–Kirchhoff stress tensor, $\tau^j_i = J\sigma^j_i$ are the components of the Kirchhoff stress tensor, and J is the Jacobian of the deformation gradient. As emphasized in (Marsden and Hughes, 1994), the definition of deformation gradient is in terms of the partial derivative instead of a covariant derivative, which is expressed as

$$F^i_J = \frac{\partial x^i}{\partial X^I}(X), \tag{19}$$

where X^I and x^i denote the reference and spatial coordinate systems respectively. For a cylindrical coordinate system, with (R, Θ, Z) and (r, θ, z) denoting the reference and spatial coordinates, the deformation gradient in matrix form is given by

$$[F^i_J] = \begin{bmatrix} \frac{\partial r}{\partial R} & \frac{\partial r}{\partial \Theta} & \frac{\partial r}{\partial Z} \\ \frac{\partial \theta}{\partial R} & \frac{\partial \theta}{\partial \Theta} & \frac{\partial \theta}{\partial Z} \\ \frac{\partial z}{\partial R} & \frac{\partial z}{\partial \Theta} & \frac{\partial z}{\partial Z} \end{bmatrix}. \tag{20}$$

The following key results are then obtained by linearizing terms in Eqs. (12)–(18) (see Appendix A for elaboration on the procedure):

$$\Delta_u(F^a_A) = \Delta u^a_{;A}, \tag{21}$$

$$\Delta_u(w^a_{;A}) = \Delta_u(\gamma^a_{bc} w^b F^c_A) + \gamma^a_{bc} w^b_{;A} \Delta u^c, \tag{22}$$

$$\Delta_u(u^i_{;j}) = \Delta(u^i_{;j}) + \gamma^i_{ab} u^a_{;j} \Delta u^b - \gamma^a_{jb} u^i_{;a} \Delta u^b, \tag{23}$$

where γ denotes the Christoffel symbol for a general curvilinear coordinate system. It is important to point out that linearization of the terms associated with the weighting function $\boldsymbol{w}$ (see Eq. (22)) is trivial in a Cartesian coordinate system. Assuming a hyperelastic material model, G_1^{int} formulated in a cylindrical coordinate system can be linearized as

$$\begin{aligned} \Delta G_1^{\text{int}} = \Delta_u G_1^{\text{int}} = & \underbrace{\int_{\Omega_0} w^i_{;j} c^{jl}_{ik} \Delta u^k_{;l} \, \mathrm{d}\Omega_0}_{\text{material term}} + \underbrace{\int_{\Omega_0} w^a_{;j} g_{ai} \tau^{jk} \Delta u^i_{,k} \, \mathrm{d}\Omega_0 + \int_{\Omega_0} w^r \tau^{\theta\theta} \Delta u^r \, \mathrm{d}\Omega_0}_{\text{conventional geometric term}} \\ & \underbrace{+ 2\int_{\Omega_0} r w^\theta_{,k} \tau^{\theta k} \Delta u^r \, \mathrm{d}\Omega_0 + 2\int_{\Omega_0} r w^r \tau^{\theta k} \Delta u^\theta_{,k} \, \mathrm{d}\Omega_0}_{\text{additional geometric term}}, \end{aligned} \tag{24}$$

where c^{jl}_{ik} are the mixed components of the fourth order spatial elasticity tensor, and $\boldsymbol{\tau}$ refers to the Kirchhoff stress tensor, to be discussed further in Section 4. Appendix A can again be consulted for more

details on the derivation of Eq. (24). The *additional geometric terms* in the above equation are due to the aforementioned linearization of $w_{i;I}$, and are *necessary* to obtain robust and rapid convergence behavior.

The second term in Eq. (12) can be rewritten in the reference geometry as

$$G_2^{\text{int}} = \int_{\Omega_0} w^i p_{,i} J \, \mathrm{d}\Omega_0. \tag{25}$$

Linearizing this term gives

$$\Delta G_2^{\text{int}} = \int_{\Omega_0} w^i \Delta p_{,i} J \, \mathrm{d}\Omega_0 - \int_{\Omega_0} w^i p_{,a} \Delta u^a_{,i} J \, \mathrm{d}\Omega_0 + \int_{\Omega_0} w^i p_{,i} \Delta u^k_{,k} J \, \mathrm{d}\Omega_0. \tag{26}$$

Considering now G_3^{int}, one can write

$$G_3^{\text{int}} = \int_{\Omega_0} q v^i_{;i} J \, \mathrm{d}\Omega_0. \tag{27}$$

Taking the directional derivative gives

$$\Delta G_3^{\text{int}} = \int_{\Omega_0} q \Delta v^i_{;i} J \, \mathrm{d}\Omega_0 - \int_{\Omega_0} q v^i_{,a} \Delta u^a_{,i} J \, \mathrm{d}\Omega_0 - \int_{\Omega_0} \frac{1}{r^2} q v^r \Delta u^r J \, \mathrm{d}\Omega_0 + \int_{\Omega_0} q v^i_{;i} \Delta u^j_{;j} J \, \mathrm{d}\Omega_0. \tag{28}$$

Applying a backward Euler difference approximation to represent the solid velocity term, this equation can be rewritten as

$$\begin{aligned} \Delta G_3^{\text{int}} = {} & \frac{1}{\Delta t} \int_{\Omega_0} q \Delta u^i_{;i} J \, \mathrm{d}\Omega_0 - \frac{1}{\Delta t} \int_{\Omega_0} (u^i_{n+1,a} - u^i_{n,a}) \Delta u^a_{,i} J \, \mathrm{d}\Omega_0 - \frac{1}{\Delta t} \int_{\Omega_0} \frac{1}{r^2} q (u^r_{n+1,a} - u^r_{n,a}) \Delta u^r J \, \mathrm{d}\Omega_0 \\ & + \frac{1}{\Delta t} \int_{\Omega_0} q (u^i_{n+1;i} - u^i_{n;i}) \Delta u^j_{;j} J \, \mathrm{d}\Omega_0. \end{aligned} \tag{29}$$

Finally, f_4^{int} can be represented in reference coordinates via

$$G_4^{\text{int}} = \int_{\Omega_0} q_{,i} k^{ij} p_{,j} J \, \mathrm{d}\Omega_0. \tag{30}$$

Assuming an isotropic permeability tensor with a constant permeability coefficient k_0, this term is linearized as

$$\begin{aligned} \Delta G_4^{\text{int}} = {} & \int_{\Omega_0} q_{,i} k^0 \delta^{ij} \Delta p_{,j} J \, \mathrm{d}\Omega_0 - \int_{\Omega_0} q_{,a} k^0 \delta^{jk} p_{,j} \Delta u^a_{,k} J \, \mathrm{d}\Omega_0 - \int_{\Omega_0} q_{,a} k^0 \delta^{ab} p_{,k} \Delta u^k_{,b} J \, \mathrm{d}\Omega_0 \\ & + \int_{\Omega_0} q_{,i} k^0 \delta^{ij} p_{,j} \Delta u^a_{,a} J \, \mathrm{d}\Omega_0. \end{aligned} \tag{31}$$

4. Hyperelastic modeling of the solid phase

In the examples to be considered in this work, the above nonlinear formulation is considered in conjunction with a Neo-Hookean hyperelastic material model for the solid phase, defined by the following equation

$$W(I_C, J) = \tfrac{1}{2}\mu(I_C - 3 - 2\ln J) + \tfrac{1}{2}\lambda(J-1)^2, \tag{32}$$

where $I_C = \operatorname{tr}\mathbf{C}$ and $J^2 = \det \mathbf{C}$ are the first and third invariants of the right Cauchy–Green deformation tensor $\mathbf{C}$. The second Piola–Kirchhoff stress is then given by

$$S^{AB} := \frac{\partial W}{\partial C_{AB}} = \mu(G^{AB} - (C^{-1})^{AB}) + \lambda J(J-1)(C^{-1})^{AB}, \tag{33}$$

where $C_{AB} := g_{ab}F^a_A F^b_B$ are the covariant components of the right Cauchy–Green deformation tensor, and G^{AB} are the contravariant components of the metric tensor in material coordinates. The Kirchhoff stress, which is a push forward of the second Piola–Kirchhoff stress, is defined as

$$\tau^{ab} = \mu(b^{ab} - g^{ab}) + \lambda J(J-1)g^{ab}, \tag{34}$$

where $b^{ab} := G^{AB}F^a_A F^b_B$ are the contravariant components of the left Cauchy–Green deformation tensor, and g^{ab} are the contravariant components of the metric tensor in spatial coordinates. Components of the spatial elasticity for this material model tensor are given by

$$c^{jl}_{ik} = \lambda J(2J-1)g^j_i g^l_k + J\left(\frac{\mu}{J} - \lambda(J-1)\right)(g_{ik}g^{jl} + g^l_i g^k_j). \tag{35}$$

Most aspects of the finite element implementation of this model are straightforward once the fully coupled linearization of the weak form is developed, as was done in the last section. The interested reader should consult standard references on the analogous problem of fully nonlinear thermoplasticity (Simo and Miehe, 1992) for details pertaining to element programming. We defer discussion of these details here, other than to remark that in a finite element context, a matrix form of the material moduli is much more convenient for numerical computation than is the fourth order tensor representation of material stiffness. Accordingly, the material stiffness term in Eq. (24) can be rewritten in an equivalent form

$$w^i_{;j}c^{jl}_{ik}\Delta u^k_{;l} = [\nabla \boldsymbol{w}]^{\mathrm{T}}_{\mathrm{vect}}\boldsymbol{D}[\nabla(\Delta \boldsymbol{u})]_{\mathrm{vect}}, \tag{36}$$

where the indicated *vector representations* of $\nabla \boldsymbol{w}$ and $\nabla(\Delta \boldsymbol{u})$ are given (using $\nabla(\Delta \boldsymbol{u})$ as an example) via

$$[\nabla(\Delta \boldsymbol{u})]_{\mathrm{vect}} := \left[\Delta u^r_{;r} \quad \Delta u^\theta_{;\theta} \quad \Delta u^z_{;z} \quad \Delta u^\theta_{;z} \quad \Delta u^z_{;r} \quad \Delta u^r_{;\theta} \quad \Delta u^\theta_{;r}\right]^{\mathrm{T}}. \tag{37}$$

With these definitions, the reduced index representation of the neo-Hookean moduli is

$$\boldsymbol{D} = \begin{bmatrix} c_1+c_2 & c_1 & c_1 & 0 & 0 & 0 & 0 \\ c_1 & c_1+c_2 & c_1 & 0 & 0 & 0 & 0 \\ c_1 & c_1 & c_1+c_2 & 0 & 0 & 0 & 0 \\ 0 & 0 & 0 & 0.5r^2c_2 & 0 & 0 & 0 \\ 0 & 0 & 0 & 0 & 0.5c_2 & 0 & 0 \\ 0 & 0 & 0 & 0 & 0 & 0.5\frac{1}{r^2}c_2 & 0.5c_2 \\ 0 & 0 & 0 & 0 & 0 & 0.5c_2 & 0.5\frac{1}{r^2}c_2 \end{bmatrix}, \tag{38}$$

where $c_1 = \lambda J(2J-1) + 2J(\mu/J - \lambda(J-1))$ and $c_2 = 2.0J(\mu/J - \lambda(J-1))$. Note that in a finite deformation torsional formulation, the unknown displacement in the θ direction is taken to be in radians, as opposed to being the out of plane displacement in a small strain formulation. This leads to the fact that $u^r_{;\theta} \neq u^\theta_{;r}$, meaning that the matrix $\boldsymbol{D}$ is 7×7 instead of 6×6.

5. Numerical and experimental investigation of torsional relaxation

The theoretical formulation described above has been used to predict the stress-relaxation behavior of articular cartilage as an example of a biphasic material, subjected to torsional deformation. A uniform mesh (Fig. 2) having 50 bilinear elements in the radial direction was used to model one-quarter of the axisymmetric cylindrical sample depicted in Fig. 1. The boundary conditions and material constants were chosen to represent torsion of a cylindrical sample of articular cartilage, similar to experiments performed

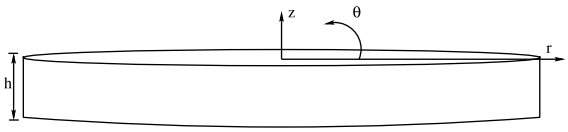

Fig. 1. Geometry of cylindrical sample modeled here. θ denotes the angle of torsional displacement imposed to achieve shear strain γ.

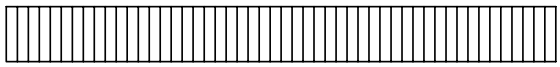

Fig. 2. The finite element mesh modeling an r–z cross section of the sample.

Table 1
Parametric cases studied with the nonlinear torsional FEM code

	t_0 (s)	d/h	λ_s (MPa)	μ_s (MPa)	θ_0	k_0 (m^4/Ns)
Case A	0.05	10	0.1	0.1, 1.0, 5.0	0.1	10^{-14}
Case B	0.05	10	0.1	0.1	0.02, 0.1, 0.2	10^{-14}
Case C	0.05	10	0.1	0.1	0.1	10^{-14}, 10^{-15}, 10^{-16}, 10^{-17}
Case D	0.05	10, 7, 3	1.0	0.1	0.1	10^{-14}

in our laboratory. The baseline parameters used to simulate the torsion experiment are provided in Table 1. The boundary conditions demand that at the upper and lower surfaces of the disk, the material be constrained in the z direction, be free to displace in the r direction, and that there be no fluid flux (i.e., the testing platens are impermeable). Angular deformation as depicted in Fig. 3 was applied to the upper surface to produce the desired magnitude of shear strain ($\gamma_0 = 0.1$) and the lower surface was fixed. Sensitivity studies were performed to determine the effect of individual parameters on the total axial stress (see Table 1). In Study A, the shear modulus of the solid matrix was varied over a range of three orders of magnitude, while in Study B, the magnitude of the shear strain applied to the biphasic material was varied from small to finite strain. In Study C, the effect of the variation in permeability over four orders of magnitude was studied. In Study D, the effect of sample aspect ratio was investigated.

The parametric studies were used to determine the ability of the FE code to model nonlinear, biphasic material behaviors and were motivated by experimentally observed results for nonlinear coupled shear and

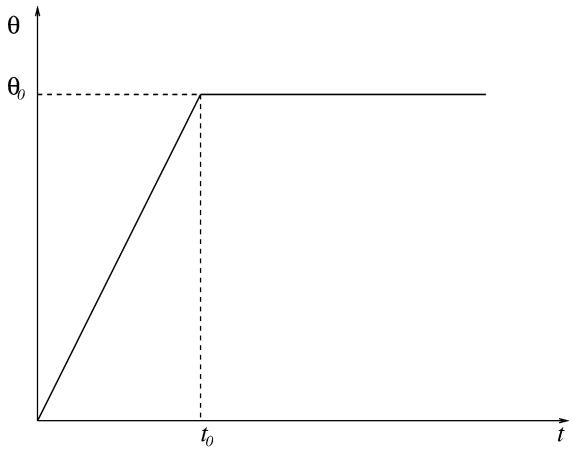

Fig. 3. The load curve.

normal stress effects in articular cartilage. Torsional experiments were performed on samples of articular cartilage from the tibial plateau of the canine knee joint, as described previously (LeRoux et al., 2000). Cylindrical samples were tested using a strain-controlled rheometer that allowed simultaneous acquisition of torque and normal force on the upper surface of the sample. The samples were compressed between impermeable, adhesive platens under strains of 12% and 20% to clamp the sample for complete torque transfer and to ensure uniform contact. The samples underwent shear deformation applied in a fast ramp (60 ms) to apply a shear strain of 0.10. For characterization of the stress-relaxation behaviors, the shear and normal stress data were individually fit to a single exponential model ($c = c_0 + c_1 e^{-t/\tau}$) for the first 100 s of stress relaxation, providing the peak stress response ($c_0 + c_1$) and characteristic time constant τ of decay.

5.1. Numerical results

The finite element code was observed to predict a nonlinearly coupled shear and normal stress-relaxation process. The model predicted rapid fluid pressurization in response to torsional deformation, which slowly decayed after a period of maintained pressurization. The normal (or axial) stress slowly increased from zero, as the total stress in the material was transferred from the fluid to the solid phase.

5.1.1. Parametric study results: case A

In general, increasing the shear modulus resulted in a decrease in the fluid pressure relative to the equilibrium shear stress, although the absolute magnitude of the fluid pressurization was higher for the materials with higher moduli (Fig. 4). The same trend was observed with respect to the effective normal stress (Fig. 5). The fluid pressure also decayed slightly more rapidly as the modulus increased. The peak pressure was the same for all cases when normalized to the equilibrium shear stress.

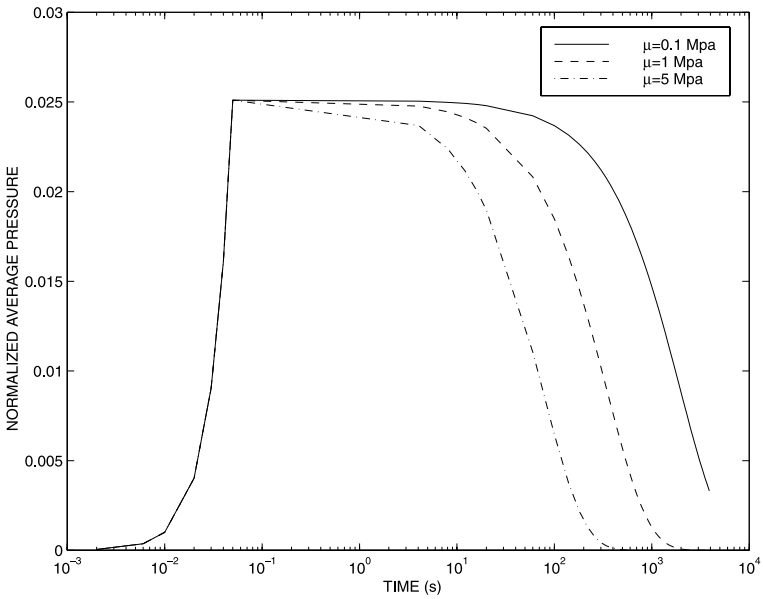

Fig. 4. Effect of shear modulus on fluid pressure, $p' = \int p \mathrm{d}A/(A_0 \times \tau_0)$, where τ_0 is the maximum equilibrium shear stress and A_0 is the area of the sample top surface.

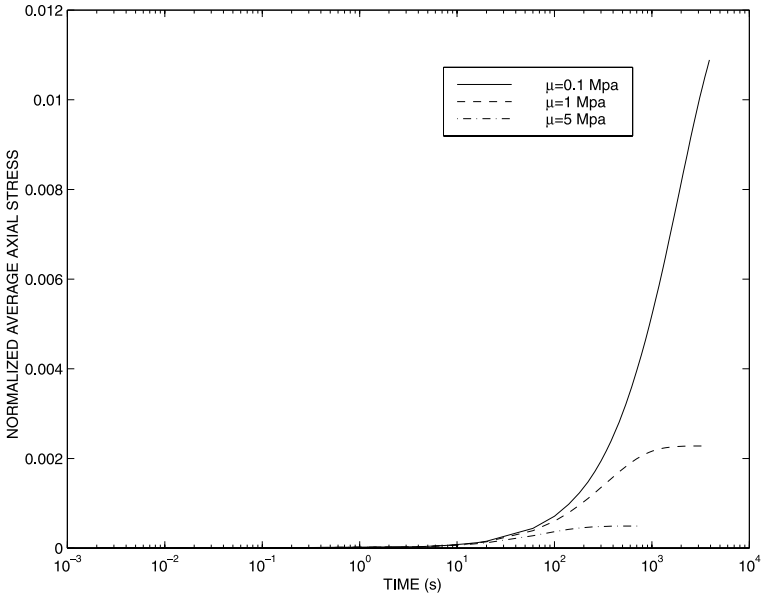

Fig. 5. Effect of shear modulus on normal stress, $\sigma_{zz}^{sf} = -\int \sigma_{zz}^{s}\,dA/(A_0 \times \tau_0)$, where τ_0 is the maximum equilibrium shear stress and A_0 is the area of the sample top surface.

5.1.2. Parametric study results: case B

These results demonstrated that the magnitude of the shear strain affected the magnitude of the total stress and effective normal stress predicted to occur in the sample (Figs. 6 and 7). The total stresses generated in the axial direction were low for small strains ($\theta_0 = 0.02$). With increasing shear strains, nonlinear effects in the axial direction developed. For the highest shear strain applied, ($\theta_0 = 0.2$), the peak total stress was one-fourth of the shear stress.

5.1.3. Parametric study results: case C

Decreasing the permeability was observed to linearly increase the period of fluid pressurization (Figs. 8 and 9). The pressure decayed to 80% of the peak pressure by 1000 s for $k = 1 \times 10^{-14}$ m^4/N s, while the pressure required 1×10^6 s to decay the same amount for $k = 1 \times 10^{-17}$ m^4/N s. The permeability does not affect the final value of stress, but it does affect the time to reach equilibrium, with smaller permeability coefficients requiring longer times.

5.1.4. Parametric study results: case D

The effect of sample aspect ratio on response was studied in these simulations (Figs. 10 and 11). With the increase of the aspect ratio, the relative fluid pressure and decay time increase as a result of the longer path for fluid exudation in the radial direction. The effective normal stress acts differently over most of the simulation time, with high aspect ratios leading to lower relative effective normal stresses. However, for very late times in the relaxation process, the curves cross, reversing this trend.

5.2. Nonlinear torsional experimental testing of articular cartilage

The experimental data from a typical cartilage sample shows the coupled shear and normal stress response following torsional deformation (Fig. 12). The normal stress from the tests performed with

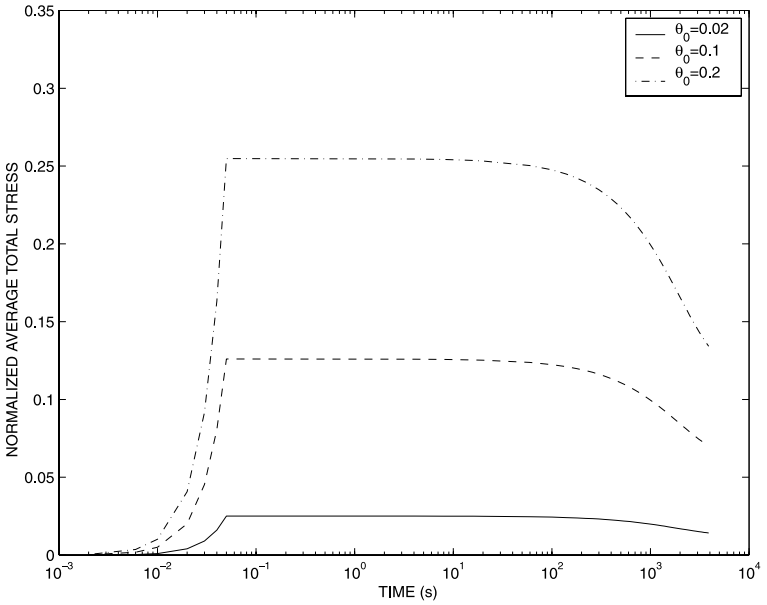

Fig. 6. Effect of shear strain on total stress, $\sigma'_{zz} = \int (p - \sigma^{s}_{zz})\,\mathrm{d}A/(A_0 \times \tau_0)$, where τ_0 is the maximum equilibrium shear stress and A_0 is the area of the sample top surface.

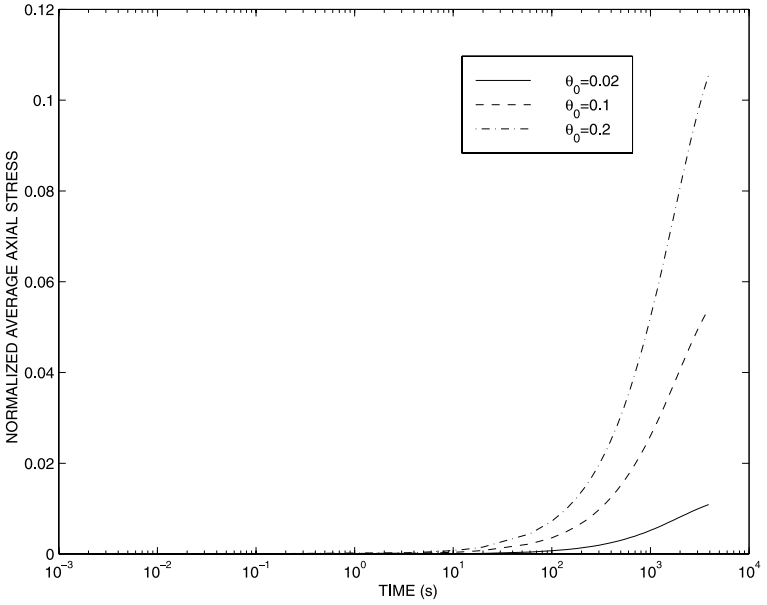

Fig. 7. Effect of shear strain on axial normal stress, $\sigma^{s\prime}_{zz} = -\int \sigma^{s}_{zz}\,\mathrm{d}A/(A_0 \times \tau_0)$, where τ_0 is the maximum equilibrium shear stress and A_0 is the area of the sample top surface.

impermeable platens is believed to correspond to the normalized total stress traction as predicted here. The peak normal stress was generally an order of magnitude less than the peak shear stress (Table 2). In 4/10

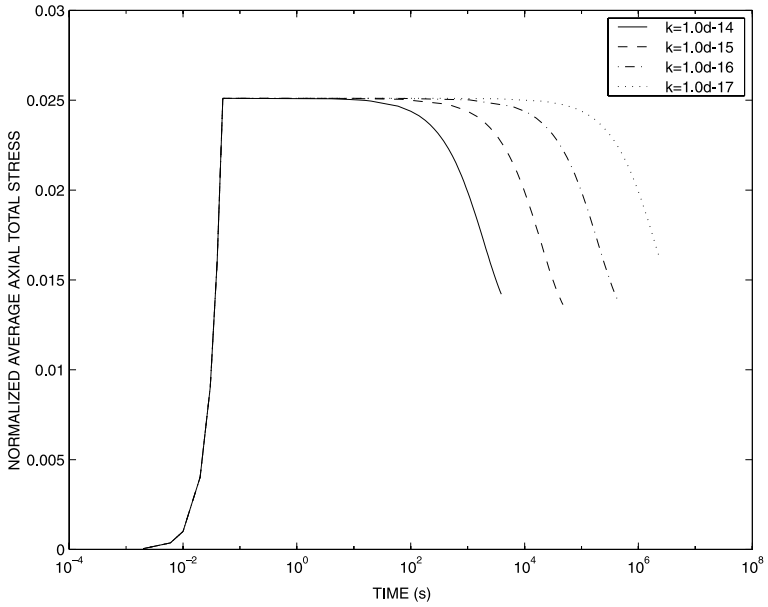

Fig. 8. Effect of permeability on total stress, $\sigma'_{zz} = \int (p - \sigma^{s}_{zz})\,\mathrm{d}A/(A_0 \times \tau_0)$, where τ_0 is the maximum equilibrium shear stress and A_0 is the area of the sample top surface.

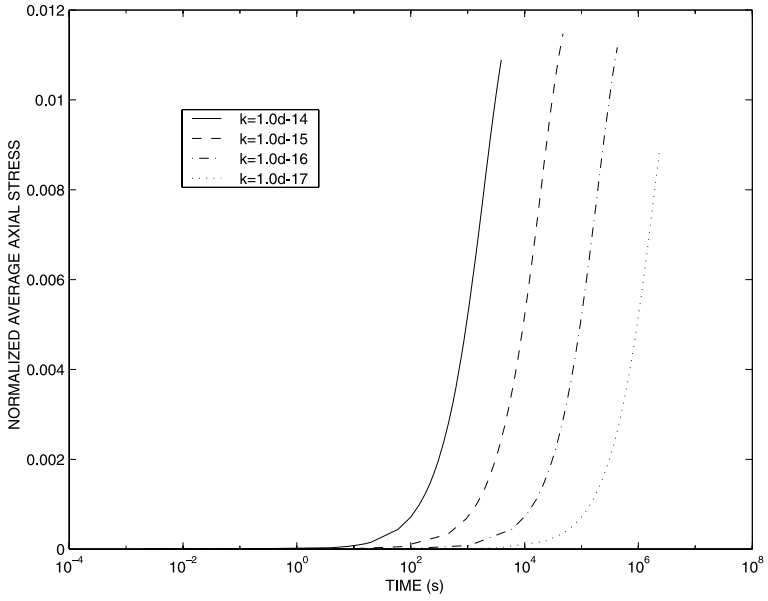

Fig. 9. Effect of permeability on normal stress, $\sigma^{s\prime}_{zz} = -\int \sigma^{s}_{zz}\,\mathrm{d}A/(A_0 \times \tau_0)$, where τ_0 is the maximum equilibrium shear stress and A_0 is the area of the sample top surface.

cases, the time constant for relaxation in shear was greater than that for the normal stress. However, the mean values for the shear and normal time constants were not significantly different (Table 2). The time

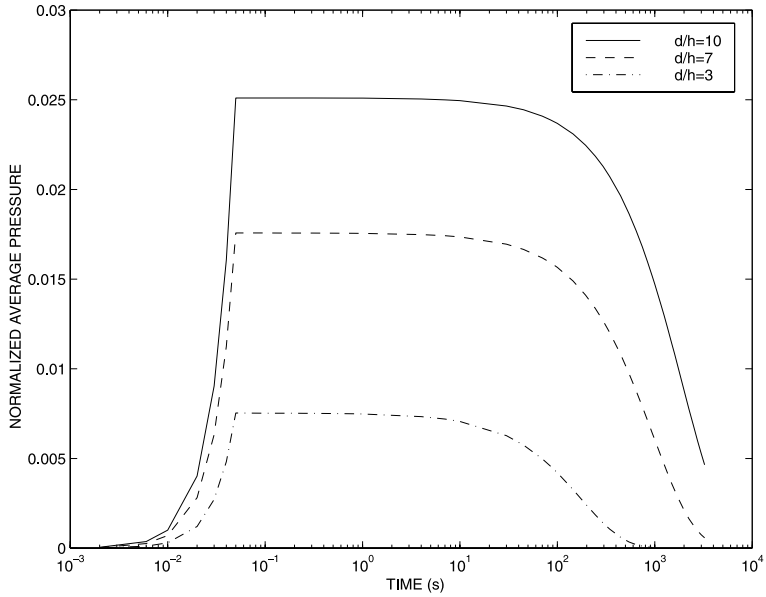

Fig. 10. Effect of aspect ratio on fluid pressure, $p' = \int p \mathrm{d}A/(A_0 \times \tau_0)$, where τ_0 is the maximum equilibrium shear stress and A_0 is the area of the sample top surface.

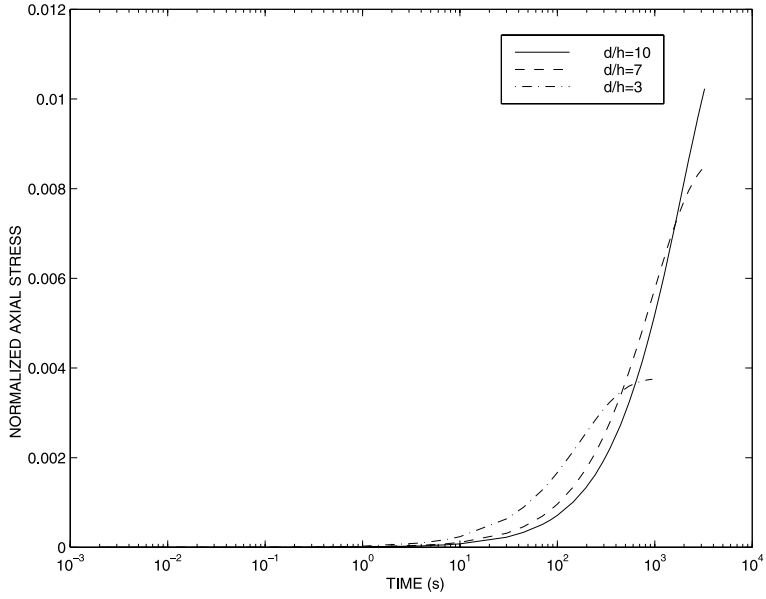

Fig. 11. Effect of aspect ratio on normal stress, $\sigma_{zz}^{s\prime} = -\int \sigma_{zz}^{s} \mathrm{d}A/(A_0 \times \tau_0)$, where τ_0 is the maximum equilibrium shear stress and A_0 is the area of the sample top surface.

constants from the fits of experimental data were short, averaging about 0.5–5 s, much less than the time for decay predicted by the computational results of at least 100 s.

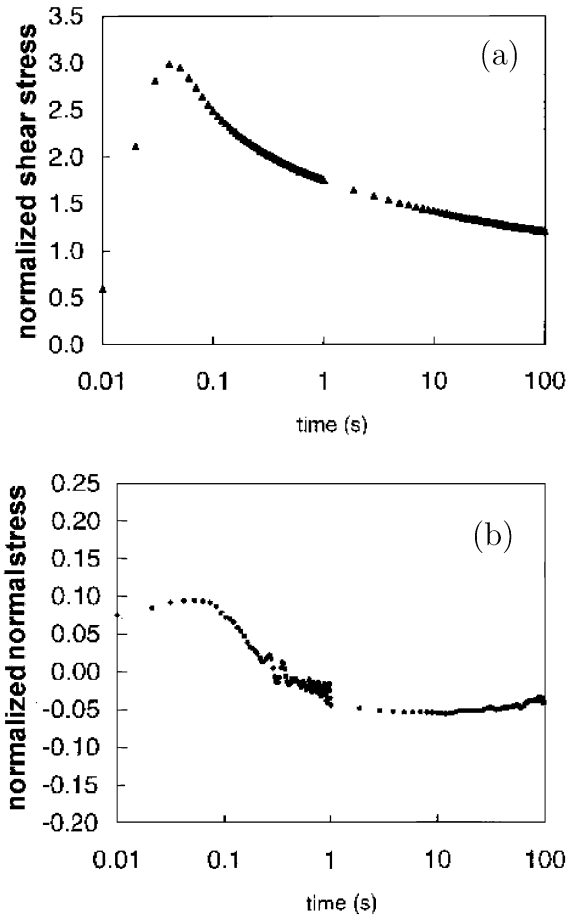

Fig. 12. Experimental stress relaxation of articular cartilage subjected to torsional deformation with $t_0 = 60$ ms, $d/h = 11.2$, $\mu = 103$ kPa and a compressive offset strain of 20%: (a) the normalized shear stress is calculated as the maximum shear stress (i.e., τ @ $r = d/2$) divided by the equilibrium shear stress, (b) the normalized normal stress was calculated as the measured axial force divided by sample area A_0, and normalized to the equilibrium shear stress. Note that the normal stress is shown as the change from the equilibrium compressive offset stress.

Table 2
Experimental results for torsion of articular cartilage with $\gamma_0 = 0.1$ and $d/h = 7.4 \pm 2.4$ (mean $\pm$ SD)

compressive offset strain	μ (kPa)	Shear		Normal	
		Peak shear stress (kPa)	τ (s)	Peak normal stress (kPa)	τ (s)
12% $n = 9$	26.8 ± 17.1	6.1 ± 3.6	0.44 ± 0.17	0.80 ± 0.50	1.2 ± 0.96
20% $n = 10$	46.0 ± 28.9	9.5 ± 5.5	0.57 ± 0.39	1.20 ± 1.90	4.3 ± 8.16

6. Conclusion

A torsional axisymmetric finite element formulation for large strain biphasic behavior has been developed, which predicts that fluid pressurization occurs simultaneously with shear stress generation when a

material undergoes shear deformation at finite strain levels. This effect, which is observed experimentally and which cannot be predicted using kinematically linear models, is felt to be important in the successful prediction and understanding of time dependent load-bearing behaviors of articular cartilage.

The finite element formulation consists of a nonlinear hyperelastic material model, torsional axisymmetric strain displacement matrices, and a novel linearization of the weak form of the variational equations. The predictions obtained from this model describe qualitatively the experimentally observed transient evolution of the normal stress that evolves in torsion testing of articular cartilage. The finite element results suggest that the total normal stress arises predominantly from fluid pressurization during the majority of the stress-relaxation process, and exhibits significant stresses in the normal direction that are nevertheless smaller than their experimentally observed counterparts.

The permeability of articular cartilage is on the order of 10^{-15} $m^4/N\,s$ (Armstong and Mow, 1982). According to the finite element simulations, performed with properties similar to those determined from experimental tests of cartilage, the theory overpredicts the time needed for stress relaxation. The low values for shear moduli and permeability coefficient determined from experiment are among the factors contributing to the discrepancy in decay times. If the experimentally determined properties are indeed representative of the true behavior of articular cartilage, then constitutive laws other than the Neo-Hookean model used here may be needed to reconcile experiment and finite element predictions, and will be the focus of future work. Furthermore, a more sophisticated nonlinear constitutive model is necessary, perhaps incorporating intrinsic viscoelasticity of the solid phase, to simulate the transient shear stress response observed experimentally.

Acknowledgements

The authors' work on this project was partially supported by the National Science Foundation under award number CMS-9703356 (Meng and Laursen), and the National Institute of Health under award numbers NIH IRO1AR47442 and IRO1AR45644 (LeRoux and Setton). Michelle LeRoux's work was partially funded by an NSF predoctoral fellowship. This support is gratefully acknowledged.

Appendix A

In this appendix, we give more details on the derivation of Eqs. (22)–(24). Employing the concept of covariant differentiation, one may write

$$\Delta(w^a_{;A} e_a \otimes E^A) = \Delta(w^a_{;A}) e_a \otimes E^A. \tag{A.1}$$

Expansion of the left hand side of this equation leads to

$$\Delta(w^a_{;A} e_a \otimes E^A) = \Delta(w^a_{;A}) e_a \otimes E^A + w^a_{;A} \Delta e_a \otimes E^A = (\Delta(w^a_{,A} + \gamma^a_{bc} w^b F^c_A) + \gamma^a_{bc} w^b_{;A} \Delta u^c) e_a \otimes E^A. \tag{A.2}$$

Since $\boldsymbol{w}$ is a weighting function, we have that $\Delta(w^a_{,A}) = 0$. Comparison of Eqs. (A.1) and (A.2) leads to Eq. (22). Following the same concept, Eq. (23) can also be derived.

From Eq. (18), we can write

$$\begin{aligned}\Delta(G_1^{\text{int}}) &= \int_{\Omega_0} \Delta(w_{i;I} F^i_J S^{JI})\, \mathrm{d}\Omega_0 \\ &= \int_{\Omega_0} w_{i;I} F^i_J \Delta(S^{JI})\, \mathrm{d}\Omega_0 + \int_{\Omega_0} w_{i;I} \Delta(F^i_J) S^{JI}\, \mathrm{d}\Omega_0 + \int_{\Omega_0} \Delta(w_{i;I}) F^i_J S^{JI}\, \mathrm{d}\Omega_0.\end{aligned} \tag{A.3}$$

A straightforward manipulation yields that

$$\int_{\Omega_0} w_{i;I} F^i_J \Delta(S^{JI})\,\mathrm{d}\Omega_0 = \int_{\Omega_0} w^i_{;j} c^{jl}_{ik} \Delta u^k_{;l}\,\mathrm{d}\Omega_0, \tag{A.4}$$

and

$$\int_{\Omega_0} w_{i;I} \Delta(F^i_J) S^{JI}\,\mathrm{d}\Omega_0 = \int_{\Omega_0} w^a_{;j} g_{ai} \tau^{jk} \Delta u^i_{,k}\,\mathrm{d}\Omega_0 + \int_{\Omega_0} w^a_{;j} g_{ai} \tau^{jk} \gamma^i_{kl} \Delta u^l\,\mathrm{d}\Omega_0 + \int_{\Omega_0} \gamma^a_{jl} w^l g_{ai} \tau^{jk} \Delta u^i_{,k}\,\mathrm{d}\Omega_0 + \int_{\Omega_0} \gamma^a_{jm} w^m g_{ai} \tau^{jk} \gamma^i_{kn} \Delta u^n\,\mathrm{d}\Omega_0. \tag{A.5}$$

Using Eq. (22), we can derive the following identity for a cylindrical coordinate system

$$\int_{\Omega_0} \Delta(w_{i;I}) F^i_J S^{JI}\,\mathrm{d}\Omega_0 + \int_{\Omega_0} w^a_{;j} g_{ai} \tau^{jk} \gamma^i_{kl} \Delta u^l\,\mathrm{d}\Omega_0 + \int_{\Omega_0} \gamma^a_{jl} w^l g_{ai} \tau^{jk} \Delta u^i_{,k}\,\mathrm{d}\Omega_0 + \int_{\Omega_0} \gamma^a_{jm} w^m g_{ai} \tau^{jk} \gamma^i_{kn} \Delta u^n\,\mathrm{d}\Omega_0 = \int_{\Omega_0} w^r \tau^{\theta\theta} \Delta u^r\,\mathrm{d}\Omega_0 + 2\int_{\Omega_0} r w^\theta_{,k} \tau^{\theta k} \Delta u^r\,\mathrm{d}\Omega_0 + 2\int_{\Omega_0} r w^r \tau^{\theta k} \Delta u^\theta_{,k}\,\mathrm{d}\Omega_0. \tag{A.6}$$

Combining Eqs. (A.3)–(A.6), we can verify that Eq. (24) holds.

References

Almeida, E., 1995. Finite element formulation for biological soft hydrated tissues under finite deformation, Ph.D. thesis. Rensselaer Polytechnic Institute.

Armstong, C., Lai, W., Mow, V., 1986. An analysis of the unconfined compression of articular cartilage. Journal of Biomedical Engineering 106, 165–173.

Armstong, C., Mow, V., 1982. Variations in the intrinsic mechanical properties of human articular cartilage with age, degeneration, and water content. Journal of Bone Joint Surg 64A, 88–94.

Bowen, R., 1998. Incompressible porous media models by use of the theory of mixtures. International Journal of Engineering Science 18, 1129–1148.

Celigoj, C., 1998. An assumed enhanced displacement gradient ring-element for finite deformation axisymmetric and torsional problems. International Journal for Numerical Methods in Engineering 43, 1369–1382.

Hayes, W., Mockros, L., 1973. Viscoelastic properties of human articular cartilage. Journal of Applied Physiology 31, 562–568.

LeRoux, M., Ateshian, G., Setton, L., 1999. Evidence of nonlinear coupled shear-normal stress effects in articular cartilage. Transactions of the Orthopaedic Research Society 24, 641.

LeRoux, M., Ateshian, G., Setton, L., 2000. Simultaneous changes in the mechanical properties, quantitative collagen organization and proteoglycan concentration of articular cartilage following canine meniscectomy. Journal of Orthopaedic Research 18, 383–392.

Levenston, M., Frank, E., Grodzinsky, E., 1998. Variationally derived 3-field finite element formulations for quasistatic poroelastic analysis of hydrated biological tissues. Computer Methods in Applied Mechanics and Engineering 156, 231–246.

Mak, A., 1986. The apparent viscoelastic bahavior of articular cartilage-the contributions from the intrisic matrix viscoelasticity and interstitial fluid flow. Journal of Biomedical Engineering 108, 123–130.

Mak, A., Lai, W., Mow, V., 1987. Biphasic indentation of articular cartilage-i theoretical analysis. Journal of Biomechanics 20, 703–714.

Marsden, E., Hughes, T., 1994. Mathematical Foundations of Elasticity. Dover, New York.

Mow, V., Kuei, S., Lai, W., Armstong, C., 1980. Biphasic creep and stress relaxation of articular cartilage in compression: Theory and experiments. Journal of Biomedical Engineering 102, 73–84.

Setton, L., Mow, V., Howell, D., 1995. Mechanical behavior of articular cartilage in shear in altered by transection of the anterior cruciate ligament. Journal of Orthopaedic Research 13, 473–482.

Simo, J., Miehe, C., 1992. Associative coupled thermoplasticity at finite strains: formulation, numerical analysis and implementation. Computer Methods in Applied Mechanics and Engineering 98, 41–104.

Soltz, M., Ateshian, G., 1998. Experimental verification and theoretical prediction of cartilage interstitial fluid pressurization at an impermeable contact interface in confined compression. Journal of Biomechanics 31, 927–934.

Soltz, M., Ateshian, G., 2000. Interstitial fluid pressurization during confined compression cyclical loading of articular cartilage. Annals of Biomedical Engineering 28, 150–159.

Spilker, R., Suh, J., Mow, V., 1990. Effects of friction on the unconfined compressive response of articular cartilage: a finite element analysis. Journal of Biomechanical Engineering 112, 138–146.

Suh, J., Spilker, R., Holmes, M., 1991. A penalty finite element analysis of biphasic hydrated soft tissue under large deformation. International Journal for Numerical Methods in Engineering 32, 1411–1439.

Truesdell, C., Toupin, R., 1960. The classical field theories, iii. 1. In: Flugg, S. (Ed.), Handbuch der Physik. Springer, Berlin, pp. 226–881.

Wayne, J., Woo, S.L., Kwan, M., 1991. Application of the *u–p* finite element method to the study of articular cartilage. Journal of Biomechanical Engineering 113, 397–403.

Zhu, W., Now, V., Koob, J., Eyre, D., 1995. Viscoelastic shear properties of articular cartilage and effects of glycosidase treatments. Journal of Orthopaedic Research 13, 771–781.